AIAA 2012-5058

Modeling and Estimation of the Yarkovsky Effect on Asteroid 1999 RQ 36

John P. Basart*, Erik Goetzke†, Christian Setzer‡, and Bong Wie§
Asteroid Deflection Research Center, Iowa State University, Ames, IA 50011, USA

Considerable attention has been given to analytically calculating the Yarkovsky effect on asteroids. It is thought that many of the asteroids in orbits close to the Earth were moved from outer orbits by this phenomenon. The orbital change is caused by solar heat absorption and asteroid re-radiation with a component of the radiation along the orbital path. Radiation causes a recoil force on the asteroid that can either increase or decrease the orbital velocity depending on prograde or retrograde, respectively, asteroid rotation. Executing the mathematics necessary to analytically calculate the radiated force on an asteroid is sufficiently complicated that it cannot be done without a number of approximations. Hence, we have taken a numerical approach in order to get more reliable solutions and to evaluate the accuracy of published analytical solutions. Our numerical approach uses COMSOL, the multiphysics software. After building an idealized model of an asteroid in COMSOL and incorporating heat transfer packages and surface-to-ambient radiation physics, it becomes much easier to numerically study the effects rotation period, sphere radius, and material composition have on the resultant force. Using parameters of RQ 36 with a 280 m radius, a rotation period of 15440 s, a spherically homogeneous model with specific heat at constant pressure of 600 J/(kg K), density of 2000 kg/m^3, thermal conductivity of 0.3 W/(m K), infrared surface emissivity 0.9, and optical surface absorptivity 0.9 we estimate a Yarkovsky force of 0.0843 N.

I. Introduction

There are hundreds of known asteroids whose orbits cross the Earth's orbit. One of these, asteroid 1999 (RQ_{36}) (RQ 36 henceforth) has become an object of interest because of its possible collision with Earth in the latter part of the 22^{nd}century.[1] With an aphelion distance of 1.356 AU (astronomical units) and perihelion distance of 0.897 AU, RQ36 is sufficiently close for a spacecraft mission before the date of possible collision, for which NASA is planning for retrieving material samples from its surface in 2016. The orbits of RQ36 and the Earth for August 15, 2012 are shown in Figure 1.

Many gravitational perturbations are considered when predicting a change in an asteroid's orbit, but one nongravitational effect believed to be of significance is the Yarkovsky effect. This effect is a radiative force most prominent on small, orbiting bodies. A considerable amount of effort has been

*Professor Emeritus, Dept. of Electrical and Computer Engineering, 342 Durham Center, AIAA Member.
†Research Assistant, Dept. of Aerospace Engineering, 3313 Frederiksen Ct., Ames, IA 50010.
‡Student, Dept. of Aerospace Engineering, 607 44th Ave, Amana, IA 52203-8306.
§Professor, Dept. of Aerospace Engineering, 2355 Howe Hall, AIAA Associate Fellow.

made, especially by Vokrouhlický, in finding analytic solutions[2–5] to this effect and how it influences an asteroid's orbit. Due to the inherent nonlinearity in modeling the asteroid's temperature rise from solar radiation, the theories become complex and require various assumptions for simplified solutions. More recently, however, there has been increased activity in using numerical methods to solve this problem as exemplified by Sekiya et al.,[6] and by Rozitis and Green[7,8]. In these examples there is still considerable analytic development before introducing numerical solutions to determine the temperature distribution and acting forces on the asteroid. The disadvantage of taking, or including, an analytic route in solving the Yarkovsky effect is that as the geometry becomes more complex, the solution will be too; perhaps to the point where it becomes nearly impossible to solve. Analytical solutions are important and useful for showing how the temperature fully depends upon the variables involved, but fully numerical solutions can offer more elegant results, without introducing simplifications. The work we present in this paper for determining the asteroid temperature distribution is completely numerical. We have used the multiphysics software package COMSOL[9] in implementing this as part of our solution to the Yarkovsky effect.

While solving for the temperature of a rotating asteroid we are also testing COMSOL to check its suitability for solving the asteroid heating problem. For the results presented in this paper, our model assumes the sphere to have homogenous material properties.

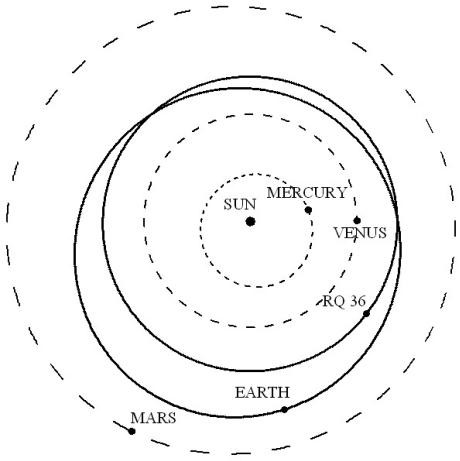

Figure 1. Orbits of Earth and RQ36 on Aug. 15, 2012.

II. Heat Transfer Theory

We follow the approach given by Vokrouhlický[10] for formulating our governing equations. We assume emission arriving from the sun is a plane wave as if emitted from a point source. When it reaches the asteroid two things happen: 1) some energy is reflected, represented by the Bond albedo $(1-\alpha)$, and 2) the remaining energy is absorbed (represented by an absorption coefficient, α). The absorbed energy heats the asteroid. The heat then flows two ways: 1) it conducts into the asteroid, and 2) the remaining heat radiates in the infrared portion of the spectrum via black-body radiation modified by an emission coefficient, ϵ. Of interest to us is this radiated heat. The infrared rays, being electromagnetic waves carry energy and momentum. The radiated momentum causes a recoil force on the asteroid. If it radiated in a direction only back towards the sun (the direction from which the solar rays came) there would be very little asteroid orbit change over a year. However, because of thermal inertia, the warmest part of the asteroid "day" is early "afternoon" as it is on the Earth if we neglect atmospheric effects. The radiation vector now has an additional component tangential to the orbit instead of only a normal component. This causes a force parallel or antiparallel to the orbit, the so-called Yarkovsky effect. (There is no reference to Yarkovsky himself since his discovery was documented only in notes.) The tangential component of radiation can either increase or decrease the size of the orbit. If the asteroid rotation is in a prograde motion with respect to the orbit, the recoil force nudges the asteroid into a higher orbit, and conversely for retrograde motion.

Our two guiding equations for determining the temperature are the heat equation

$$\rho C \frac{\partial T}{\partial t} = K \nabla^2 T \tag{1}$$

and the boundary condition

$$\epsilon\sigma T^4 + K\left(\hat{\mathbf{n}} \cdot \nabla T\right) = \alpha\varepsilon \tag{2}$$

where T is the temperature in Kelvins, ρ is the density, C the specific heat, K the thermal conductivity, t the time, σ is the Stefan-Boltzmann constant, ε is the power density from the sun at the distance of the asteroid, ∇ the gradient, and ∇^2 the Laplacian operator. $\hat{\mathbf{n}}$ is a unit vector normal to the surface. All units are in the SI system. In the second equation the temperature is to be evaluated at the boundary. If we assume heat transfer only in the radial direction, Eqs. 1 and 2 become

$$\rho C\frac{\partial T}{\partial t} = K\frac{\partial^2 T}{\partial r^2} \tag{3}$$

and

$$\epsilon\sigma T^4 + K\frac{\partial T}{\partial r} = \alpha\varepsilon. \tag{4}$$

Many journal papers dealing with the Yarkovsky effect are solving for temperature starting with these equations. The excessive difficulty solving for temperature lies with T^4 in the second equation. Our solution is strictly numerical with no further manipulations of the two equations.

III. Force Theory

Once we have the surface temperature distribution over the entire body we can calculate the force. A rigorous detailed way to do this is to use the Maxwell Stress Tensor [11, p. 239]. However, by not being concerned with the behavior of electric and magnetic fields over the body we can use the more macroscopic approach of radiative transfer [12, Chap. 3] using power as the basic quantity instead of electromagnetic fields. Our basic quantity is *specific intensity,* $I_\nu(s,\Omega)$ represented by I_ν, of radiated power in watts per meter squared per Hertz per solid angle, Ω. Surface area is represented by s. The energy, in joules, radiated from a surface ds in the θ direction (referenced to the surface normal) into a differential solid angle $d\Omega$ is

$$dE_\nu = I_\nu \cos\theta ds\, d\nu\, d\Omega\; dt. \tag{5}$$

where ν is the frequency. We next apply the quantum mechanical expression for energy

$$E^2 = p^2c^2 + m^2c^4 \tag{6}$$

where p is the momentum of a particle, c is the velocity of light in a vacuum, and m is the mass of the particle. An important property of this equation is that it applies to continuous quantities as well as to point particles. In the case of radiation we are dealing with a photon whose mass is zero. We therefore get an expression for momentum as

$$dp = dE_\nu/c = I_\nu \cos\theta ds\, d\nu\, d\Omega\; dt/c. \tag{7}$$

Now we can formulate pressure, P_r, using the definition that pressure caused by radiation is the net rate of transfer of momentum normal to, and across, ds. Thus

$$dP_r(\nu) = \frac{dp}{ds\, dt}\cos\theta. \tag{8}$$

We get the total outward pressure per unit frequency by integrating over a hemisphere:

$$P_r(\nu) = \frac{1}{c}\int I_\nu \cos^2\theta\, d\Omega = \frac{1}{c}\int_0^{2\pi}\int_0^{\pi/2} I_\nu \cos^2\theta\, \sin\theta\, d\theta\, d\phi. \tag{9}$$

Since we do not know the distribution of specific intensity over the surface, we assume it is a constant with respect to position. The pressure integral becomes

$$P_r(\nu) = \frac{I_\nu}{c} \int_0^{2\pi} \int_0^{\pi/2} \cos^2\theta \, \sin\theta \, d\theta \, d\phi = \frac{I_\nu}{c} \frac{2\pi}{3}. \tag{10}$$

To get an expression for spectral intensity, $I_{\nu,}$we assume black body radiation which is given by

$$\pi I_\nu = \frac{2h\nu^3}{c^2} \frac{1}{e^{h\nu/kt} - 1} \tag{11}$$

where h is Plank's constant. The π to the left of I_ν converts I_ν to watts per meter squared per Hertz to agree with the units of the Planck law. To find the intensity over all frequencies we integrate Planck's law and represent the result by I (no subscript). We have

$$\pi I = \int_0^\infty \frac{2h\nu^3}{c^2} \frac{1}{e^{h\nu/kt} - 1} d\nu = \sigma T^4 \tag{12}$$

with units of W/m^2. The last part of this expression is the Stefan-Boltzmann law where σ is the Stefan-Boltzmann constant. With this result we get the total pressure in the radial direction over all frequencies as

$$P_r = \int P_r(\nu) \, dv \, = \frac{2}{3c} \epsilon \sigma T^4 \tag{13}$$

in N/m^2, where we have inserted the emission coefficient, ϵ, since an asteroid is not a perfect black body radiator.

Finally we arrive at the force calculation. Given the results of the radial pressure over the entire surface of the body we discretely sum up individual contributions. The individual numbers come from a COMSOL numerical solution for temperature. We use COMSOL to find the temperature distribution and use our own software to convert the temperature to force. For each mesh segment in the temperature solution there is a temperature that is assigned a vector direction normal to the surface of the segment, $\mathbf{n}_i$. See Figure 2 for an illustration of vectors emanating normally to the mesh segments. The temperature vectors are converted to pressure using Eq. 13 and summed with the formula

$$\mathbf{F} = \sum_{i=1}^{N} P_{ri} \mathbf{n}_i A_i = \sum_{i=1}^{N} \frac{2}{3c} \epsilon_i \sigma T_i^4 \mathbf{n}_i A_i \tag{14}$$

This is the equation we used in our own software once we solved for the surface temperature distribution with the COMSOL software. Spatial force components were calculated for each segment, then components were summed vectorily with the final F_x, F_y,and F_z components used to calculate the total force magnitude and direction.

IV. COMSOL

The approach we've taken in numerically solving for the temperature associated with the Yarkovsky Effect is fully dependent upon the COMSOL Multiphysics software. The software is well organized to help the user step through the process of setting up all the inputs. The major steps in the set-up are:

1. Select Space Dimension
2. Add Physics Module(s)
3. Select Study Type
4. Build Geometry
5. Select Materials. (We set thermal conductivity $K = 0.3$, density $\rho = 2000$, heat capacity $C = 600$, absorption coefficient, $\alpha = 0.99$, and an infrared emissivity, $\epsilon = 0.9$, the same used for RQ 36 in Delbo and Michel[13])
6. Define boundary conditions
7. Build mesh
8. Execute program

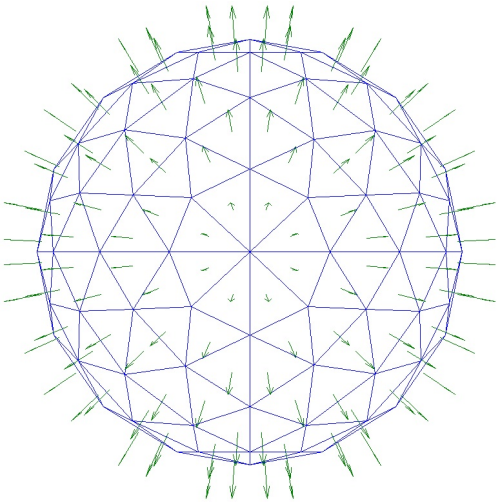

Figure 2. Vectors emanating normal to mesh segments. When written in terms of pressure they are vectorally summed to give the final force.

The working model developed with this software incorporates a three dimensional sphere working with the physics of heat transfer in solid bodies. To simulate an asteroid in space, surface-to-ambient radiation and a boundary heat source were applied to the surface of the sphere as well. The boundary heat source simulates a plane wave exposing one side of the body at a given time. For the sphere to be able to rotate while exposed to the radiation, a time-dependent study was required in which we found 30 periods of rotation to usually be a sufficient amount of time in achieving equilibrium results. Due to the limitations of finite element analysis however, the geometry does not rotate when exposed to a heat source, but considering relative motion, the boundary heat source moves about the sphere in our model with coordinate corrections done in post processing calculations to make it appear the sphere was rotating. The last thing required to simulate the temperature development of an asteroid was an initial temperature of the starting body, which, when appropriately defined, drastically cut down the number of periods of rotation required to reach equilibrium values. Most of these steps have substeps incorporated.

When working with any finite element analysis software, the type and strength of the meshing is important in achieving viable results. A free tetrahedral meshing was used here (see Figure 2 for an example of meshing with a small amount of elements) but in some cases a free triangular, swept meshing was needed, as will be described later in the results section.

One of the most important steps in building the asteroid model was to properly incorporate the boundary conditions and more specifically the moving heat source. Being that RQ36 is sufficiently far from the sun, a uniform plane wave of incoming radiation was assumed. To simulate this plane wave on the surface of the sphere, a cosine distribution was used on the model to taper the illumination from the subsolar point to the poles and limbs of the sphere. Keeping the asteroid at a distance of 1 AU from the sun, the maximum heat flux was 1378 W/m^2. As mentioned before with limits on finite element analysis, the geometry and meshing cannot move but the boundary conditions were manipulated to do so. This was done using coordinate transformations during COMSOL's iterations and then correcting this to appear as if the asteroid were rotating by counter coordinate transformations in post processing of the temperature data.

V. Results

Many different computer simulations were made in determining which of the parameters specified in the asteroid model contribute to the Yarkovsky Effect. We've found the resultant force vector and its components to be related to the size of the sphere, the period of rotation, and the obliquity

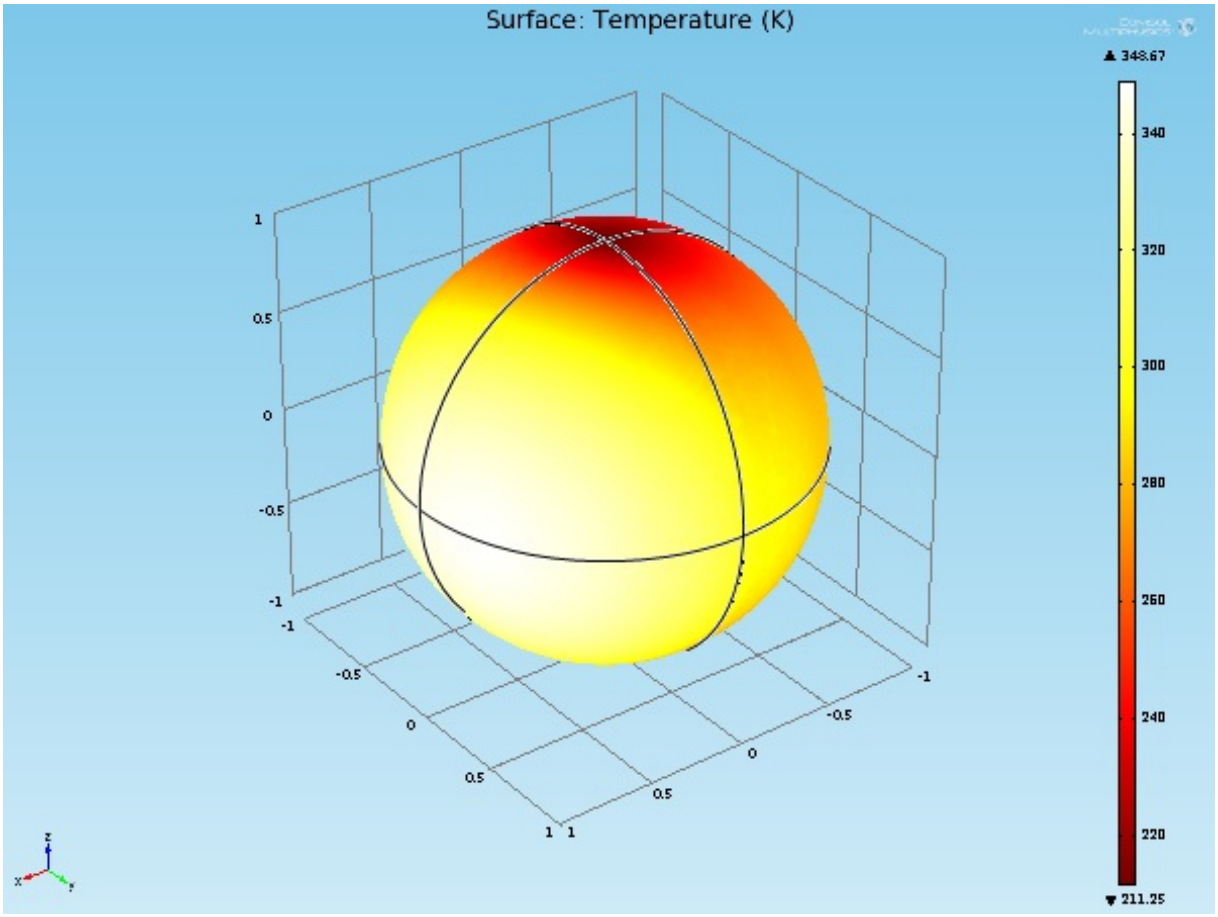

Figure 3. Graphical output of COMSOL showing a color coded temperature distribution.

of the spin vector. The relationships between force and material properties are not considered here; we left the values of thermal conductivity K, density ρ, and heat capacity, C, to match the ones representative of RQ 36, as described in the previous section. There are additional parameters required as inputs for the COMSOL simulation to run properly, but their only effects are on the length of simulation time required for achieving stable results, including initial temperature (T_0), step size, number of steps, and meshing scheme.

Before the force can be calculated, the temperature distribution on the surface of the body has to be known. Figure 3 shows a global image of the final distribution which is direct output from the COMSOL software. The hottest region (white) is clearly offset from the direction of illumination (intersection of two great circles on the left). Rotation is counterclockwise.

Figure 4 shows a typical plot of temperatures as dependent on the number of iterations where the time variable here is referenced as the number of periods elapsed for different points of interest on the spherical model. Data are plotted for four different regions on the sphere. These data were taken from a simulation involving a one-meter radius sphere, rotating with a period of 15440s ($\approx$ 4.3 hrs, the rotation period of RQ 36). Given a 90 degree obliquity in this run, the North Pole and South Pole have the same temperatures and only one of the values is reported here.

There is transient behavior in the plotted temperature data when the distribution starts to develop. As time goes on, however, these dampen out and a stable distribution is reached, usually before 30 periods of rotation. The pole temperatures are still decreasing after 30 periods of calculation and will do so for some time, but given that this simulation has a 90^0 obliquity, the

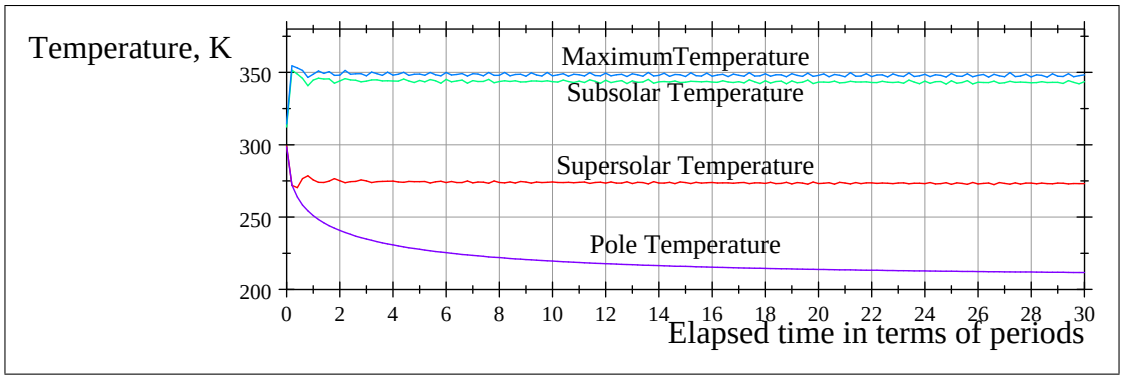

Figure 4. Plot showing temperatures on the body converging to final values.

contributions of these area's temperatures to the resultant force are canceled out by symmetry of the sphere about the equator and orbit plane.

The temperature distribution of an equatorial slice of the model is shown in Figure 5. Illumination

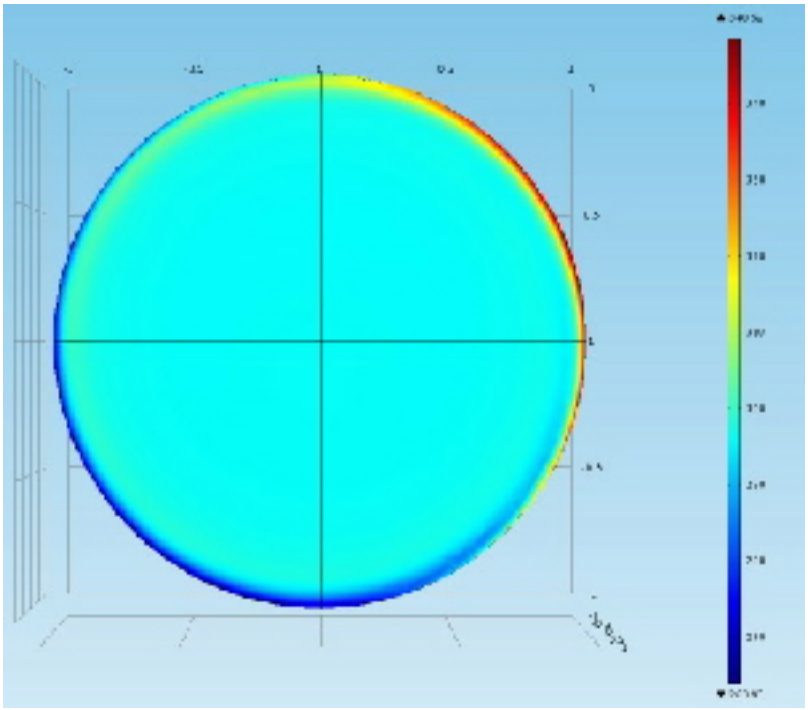

Figure 5. Equatorial cross section of temperature distribution. Rotation is CCW and solar illumination along the x-axis from the right.

is from the right. The sphere is rotating counterclockwise so the change in temperature is visible from the warm red region, early "afternoon" to the cool blue region just before "dawn". The temperature propagation into the sphere is shallow with a penetration depth roughly constant for variously sized spheres. Given this mostly radius independent penetration depth for different sized spheres, we were able to "hollow" out the sphere for larger radii to allow for finer meshing schemes on the remaining shell. This was helpful in reducing computation times given our limitations on computational resources. We found a shell thickness between one and three meters to suffice for our computations.

V.A. Initial Temperature Analysis

We experimented with various initial temperatures of the sphere to test the independence of the result upon the final temperature distribution. Figure 6 shows the results for several initial temperatures. After some length of time, the temperature distribution of the sphere becomes independent of the initial temperature assumed. Our numerous test plots extended for 30 periods of rotation to show the length of time required to reach the final temperature distribution. Depending upon the period of rotation and initial temperature chosen for the body, 30 periods may or may not be enough time. Figure 6 shows how the maximum temperature behaves on a 1 m sphere. The sphere was rotating with a period of 15440 s and positioned with 90^o obliquity. For all five temperature curves plotted, they are asymptotically approaching the same temperature, suggesting that the specified initial temperature only influences how long it takes to achieve the desired equilibrium distribution necessary for an accurate force calculation (see Eq. 14). This behavior is also representative of the temperature behavior at the subsolar, supersolar, and pole locations on the sphere. Through more rigorous analyses we found 303 K to be the initial temperature to use on a sphere with RQ 36 thermal parameters.

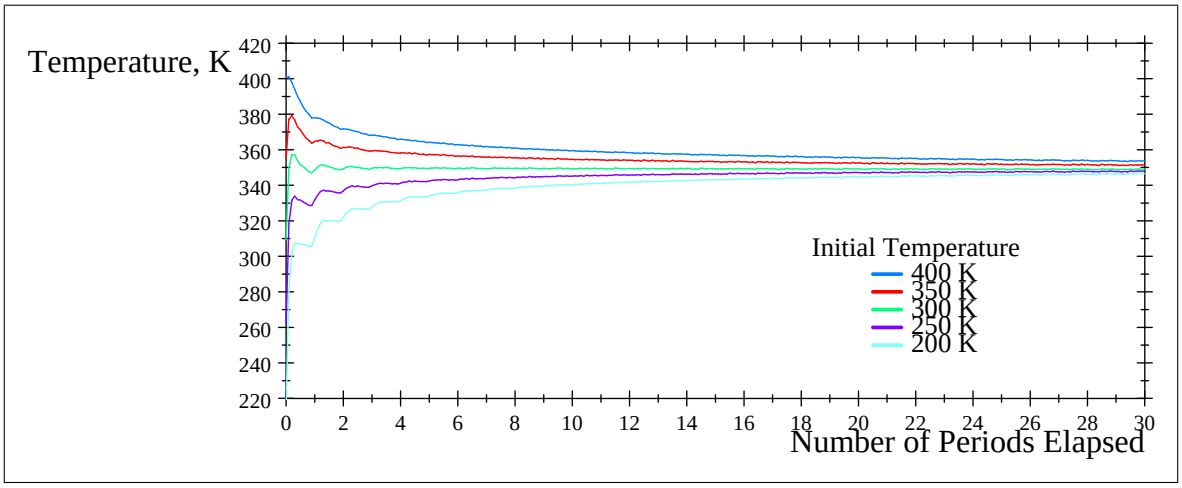

Figure 6. Convergence of maximum temperature of the hot spot for various initial values.

V.B. Equatorial Temperature Observations

As we experimented with various radii, we found that temperature has little dependence upon radius with all else being equal, a very unexpected result. Temperature does vary more strongly, however, with rotation period. In Figure 7 we show several curves for temperature over the equatorial region for combinations of three radii and two rotation periods (in seconds). Overall the curves exhibit a cooling to the right of the "hot" region and continued cooling until early morning. Then when the sun starts shining on the material coming into the dawn side, the temperature starts to climb rather abruptly for the slower rotation.

There are three blended curves at the highest peak in the graph demonstrating that for a 72000 s rotation period the subsolar equatorial temperature is independent of sphere radius. On the dawn side we see slight variations for the three different radii for this period. The other three curves are for the faster rotation period of 18000 seconds. These peaks are shifted to the right relative to the slower rotation indicating for faster rotations the hot spot moves farther away from the subsolar point as one would expect. Near the peaks of these three curves we see more radii dependence

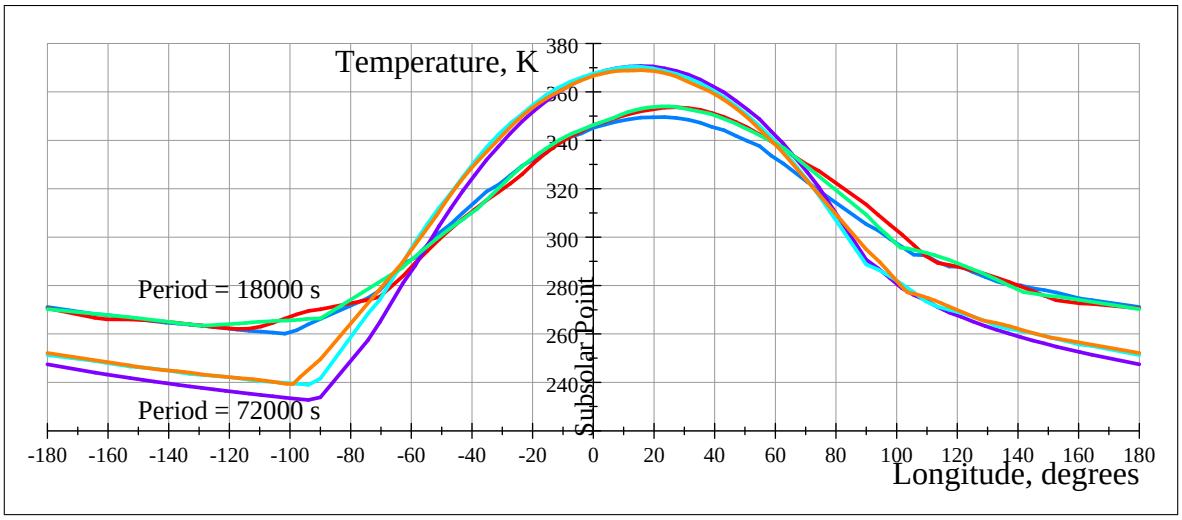

Figure 7. Equatorial temperature distributions for two different rotation periods for sphere radii of 1, 100, and 280 m.

than for the slower rotation, but this dependence dissolves as the body cools. Just before dawn they again separate slightly over a short distance. The faster rotating bodies do not heat as much as the slower rotating bodies, but they do not cool as much either. For all six curves, all physical parameters are the same except for the two parameters shown.

We fit equations to the temperature as a function of period for several locations for spheres of 1 m, 100 m, and 280 m radius. The results for the 1-m sphere as a function of period, P, were

$$T_{\max}(\text{HotSpot}) = 13.5\ln(P) + 219 \quad (15)$$

$$\text{Angle of } T_{\max}, \text{deg}. = 336P^{-0.278} \quad (16)$$

$$T_{\text{subsolar}} = 15.3\ln(P) + 195 \quad (17)$$

$$T_{\text{supersolar}} = -16.5\ln(P) + 431. \quad (18)$$

For the 100-m sphere

$$T_{\max}(\text{HotSpot}) = 13.5\ln(P) + 219 \quad (19)$$

$$\text{Angle of } T_{\max}, \text{deg}. = 1800P^{-0.444} \quad (20)$$

$$T_{\text{subsolar}} = 15.3\ln(P) + 195 \quad (21)$$

$$T_{\text{supersolar}} = -16.5\ln(P) + 431. \quad (22)$$

And for the 280-m sphere

$$T_{\max}(\text{HotSpot}) = 13.7\ln(P) + 217 \quad (23)$$

$$\text{Angle of } T_{\max}, \text{deg}. = 1450P^{-0.423} \quad (24)$$

$$T_{\text{subsolar}} = 16.7\ln(P) + 182 \quad (25)$$

$$T_{\text{supersolar}} = -13.2\ln(P) + 400. \quad (26)$$

V.C. Depth of Penetration Observations

We saw earlier in Figure 5 that the heat penetration depth was shallow. We show this more explicitly in Figures 8 and 9.

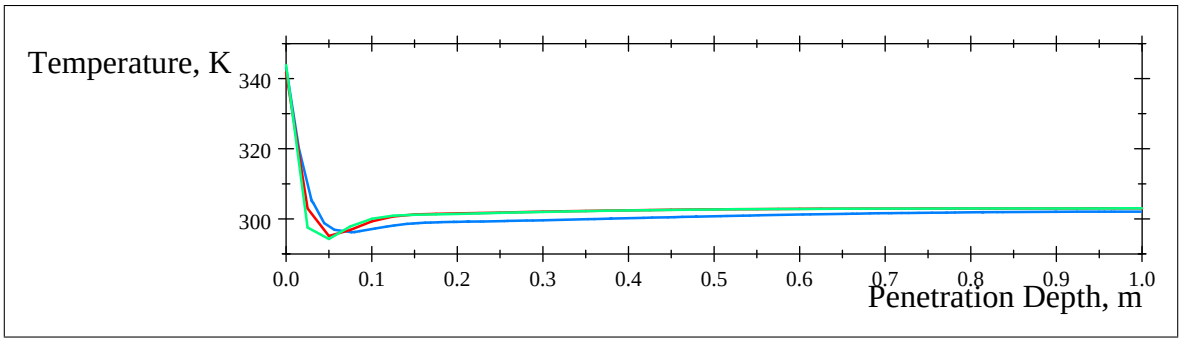

Figure 8. Penetration depth of temperature at the subsolar point (sun side).

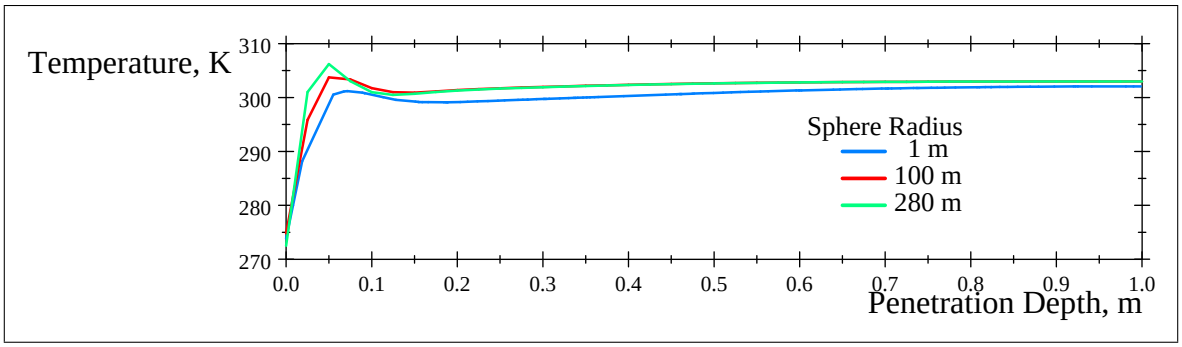

Figure 9. Penetration depth of temperature at the supersolar point (far side).

For the larger spheres in the upper figure we see a clearly defined layer where the temperature is the coolest at about 40 to 50 cm deep with a temperature of about 295 K. The small spheres tend to stay near this lower temperature while the interior of the larger spheres warms back up after the dip and settles in at 303 K. There is about a 40 K drop between the surface temperature and the interior temperature (303 K) for the larger spheres. In the night-time plot in Figure 9 we see about a 28 K drop between the interior and the surface temperature. There is a wider spread of temperatures in the dip at night than in daytime.

V.D. Force Analysis

We discuss force dependence upon five things: 1) Step size, 2) Mesh size, 3) Obliquity of the incident solar angle, 4) Period of sphere rotation, and 5) Radius of the sphere. All other parameters are the same as for RQ 36. Due to the slight fluctuations in temperature even after a large number of iterations, we obtain stable reportable numerical results by averaging the results for the last five rotation periods**.**

V.D.1. Step Size Analysis

COMSOL gives us a choice of step size in the iterations. To test the effect of step size on the temperature results we made runs with six different step sizes. Table 1 shows the results. Once the number of steps per period is greater than three, there is no change in the final force calculation. Consequently, in subsequent runs we used 10 steps per period of rotation.

Table 1. Examples of force dependence upon the number of iterations (steps).

Steps per Period	**Force, μN**
30	2.05
12	2.05
10	2.05
5	2.05
2	2.04
1	1.97

Table 2. The composite force for runs with various numbers of mesh elements.

Total No. of Elements	**No. of Surface Elements**	**Force, μN**
64	48	1.12
401	152	1.26
1136	240	1.53
2771	464	1.77
8516	848	1.98
16,726	1280	2.06
53,296	2776	2.04
208,835	6552	2.00
1,135,550	19664	2.05

V.D.2. Mesh Size Analysis

Table 2 shows the resultant force magnitude corresponding to different tetrahedral mesh settings, all on a 1-m sphere. We only report the number of total elements and surface elements here, as the names the COMSOL software has designated for the mesh settings (i.e. "Coarse", "Normal", or "Fine" meshing) are somewhat misleading. The sphere was rotating with a period of 15440 s, and a 90^o obliquity. As the table shows, the resultant force magnitude is dependent upon the number (and also the size) of the elements. For most of the data presented in this paper 53,296 elements were used. However, in some cases 1,135,550 elements were needed. This table is only for tetrahedral meshing, but we did need to use a swept meshing type for some of the calculations. Our swept meshing consisting of triangular facets layered between two surfaces was used on the large radius simulations when a hollow sphere was required to conserve computational resources.

V.D.3. Solar Obliquity Dependence

Figures 10 and 11 illustrate the dependence of the magnitude of the force versus obliquity (colatitude) of incident radiation from the sun. The colatitude, θ, is measured from the north pole (0^0) towards the equator (90^0) and ϕ, the longitude, is measured from the subsolar point. The direction angles of the force are specified by θ_F and ϕ_F.

The equations for the total force and force components in Figure 10 are

$$F_x = 2.05 \times 10^{-6} \cos(2i) + 3.72 \times 10^{-6} \quad (27)$$

$$F_y = 1.19 \times 10^{-6} \sin(i) \quad (28)$$

$$F_z = 2.09 \times 10^{-6} \sin(2i) \quad (29)$$

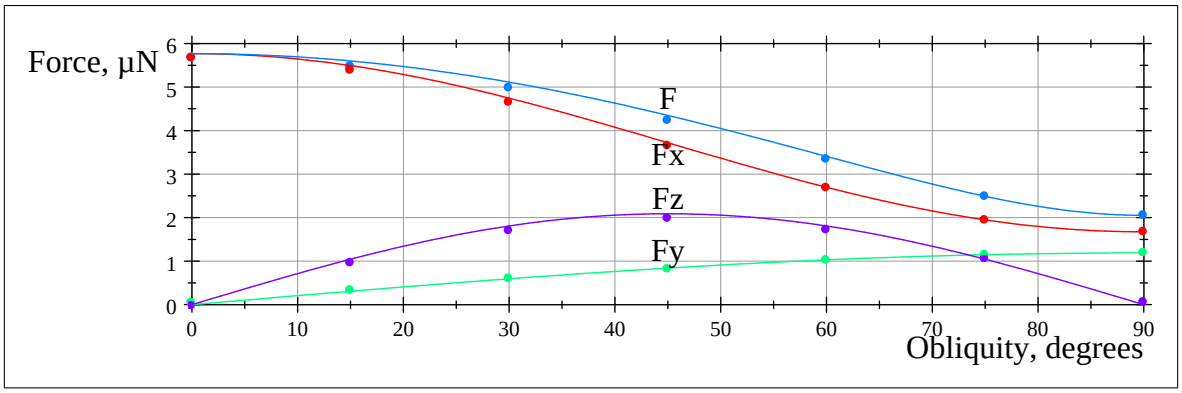

Figure 10. Total force versus colatitude of incident solar radiation.

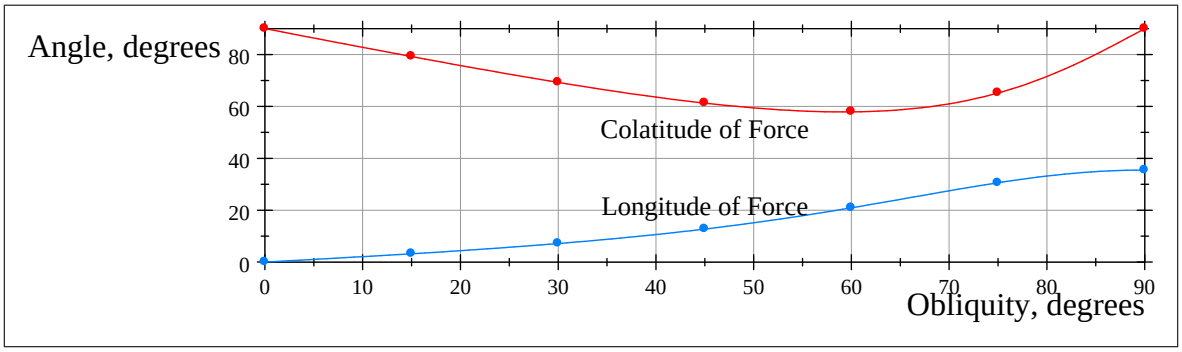

Figure 11. Direction of the force versus colatitude of incident solar radiation.

with the total force equation being

$$F = 8.27 \times 10^{-7} \sqrt{-(\cos^2(i) - 21.3)^2 + 480} \tag{30}$$

where i is in degrees. The spherical coordinate values for the angle of the force magnitude as shown in Figure 11 are

$$\phi_F = \tan^{-1}(F_y/F_x) \tag{31}$$
$$\theta_F = \cos^{-1}(F_z/F). \tag{32}$$

V.D.4. Period Dependence

Force dependence upon period for three sizes of spheres (1, 100, and 280 meters) is shown in Figures 12, 13, and 14. In general, the forces for the three spheres increase logarithmically with period as shown in the equations below that were fit to the plots.

For the one-meter sphere

$$F = 7.85 \times 10^{-7} \ln(0.000941P) \tag{33}$$
$$F_x = 8.21 \times 10^{-7} \ln(0.000609P) \tag{34}$$
$$F_y = 1.05 \times 10^{-7} \ln(0.633P) \tag{35}$$
$$F_z = 0. \tag{36}$$

For the 100-m sphere

$$F = 6.99 \times 10^{-3} \ln(0.00138P) \quad (37)$$
$$F_x = 8.09 \times 10^{-3} \ln(0.000622P) \quad (38)$$
$$F_y = 0.0101 \quad (39)$$
$$F_z = 0. \quad (40)$$

And for the 280-m sphere

$$F = 0.0542 \ln(0.00144P) \quad (41)$$
$$F_x = 0.0624 \ln(0.000645P) \quad (42)$$
$$F_y = 0.0786 \quad (43)$$
$$F_z = 0 \quad (44)$$

The smaller spheres have very similar results, but start to differ with F_y which is the Yarkovsky force (F_y is parallel to the orbit). For larger spheres, the F_y component is constant with period with our range of period analysis (3600 to 72,000 seconds or 1 to 20 hours).

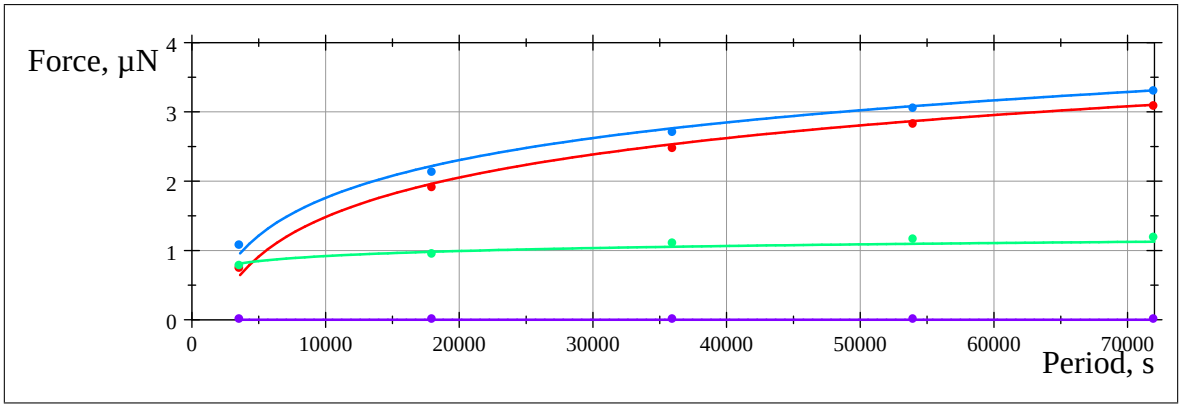

Figure 12. Force for a 1-meter sphere. Blue is the total force, red the x component, green the y component, and purple (along the bottom) the z component.

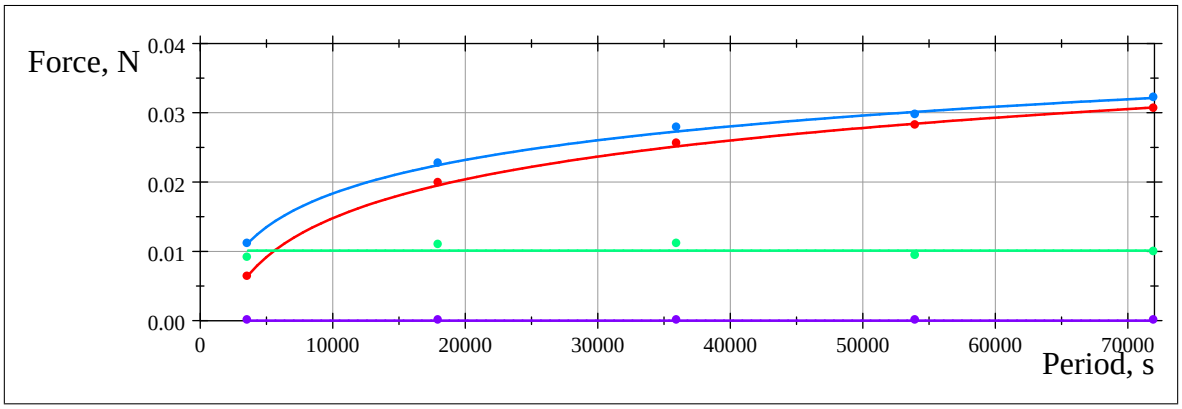

Figure 13. Force for a 100-meter sphere. Blue is the total force, red the x component, green the y component, and purple (along the bottom) the z component.

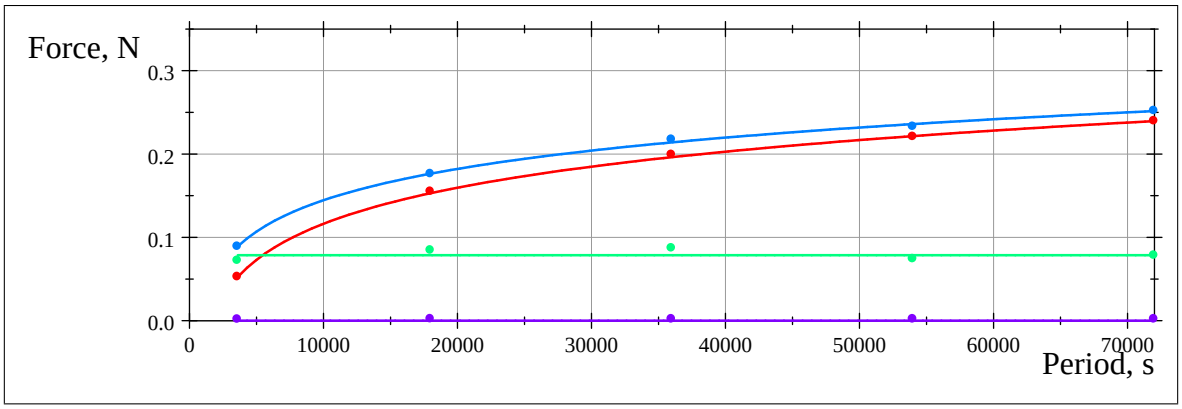

Figure 14. Force for a 280-meter sphere (size of RQ 36). Blue is the total force, red the x component, green the y compont, and purple (along the bottom) the z component.

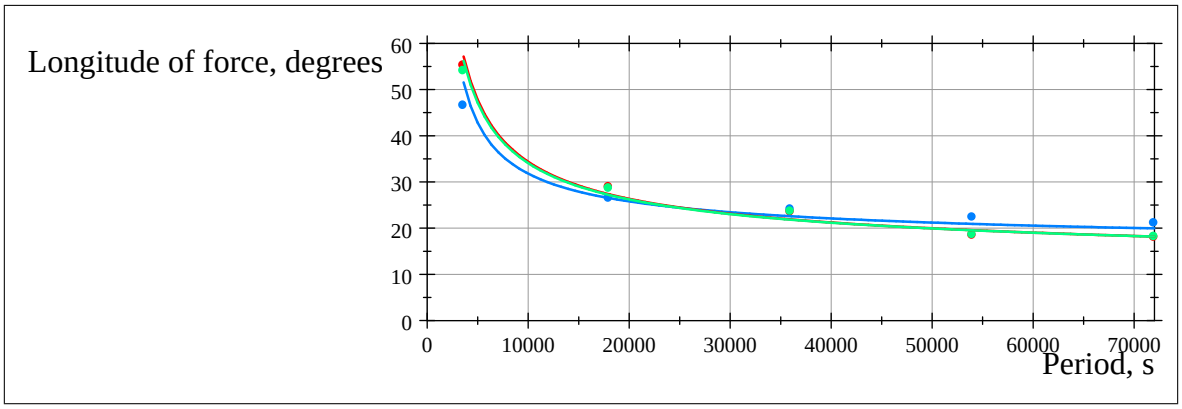

Figure 15. Angles of all forces for 1-m sphere (blue), 100-m sphere (red) and 280-m sphere (green).

V.D.5. Radius Dependence

We observed earlier that temperature is weakly dependent upon radius, hence, according to Eq. 14 the force will basically vary with area. Since area goes as r^2 we expect the force to go as r^2 which it does as we see in Figure 16.

The equations for the force are

$$F = 2.15 \times 10^{-6} r^2 \quad (45)$$

$$F_x = 1.86 \times 10^{-6} r^2 \quad (46)$$

$$F_y = 1.08 \times 10^{-6} r^2 \quad (47)$$

$$F_z = 0 \quad (48)$$

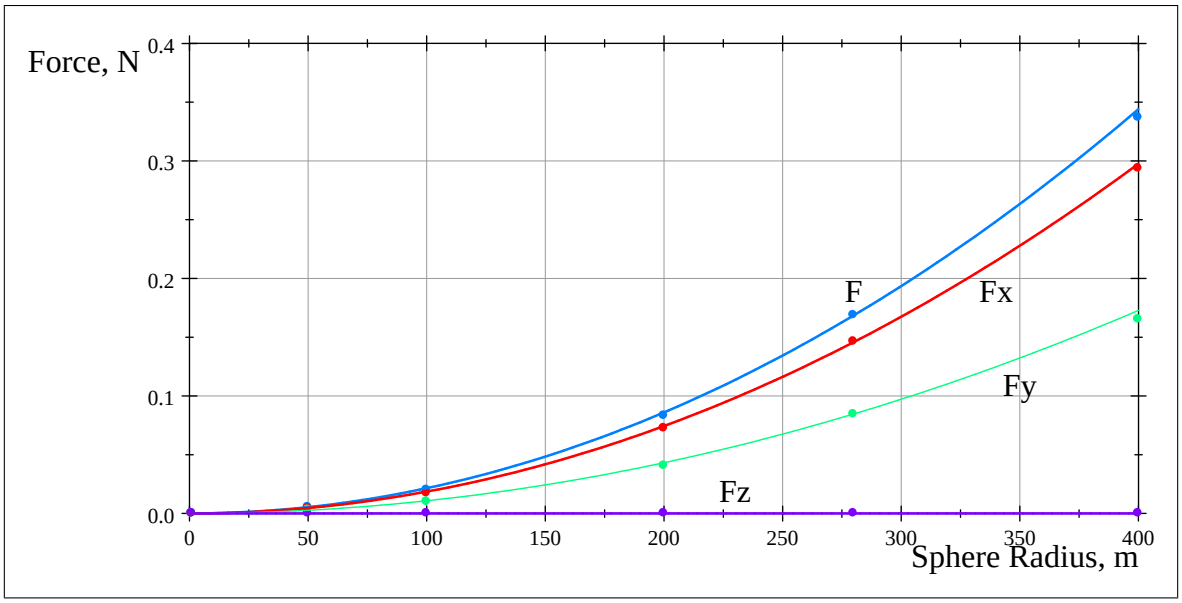

Figure 16. Plot of force demonstrating radius squared dependence.

VI. Comparison with Previously Published Forces

Sekiya et al.[6]compared their iterative results for temperature vs. longitude with results from Vokrouhlický[10] in plots in their Figures 4 and 5. We extracted numerical values from their plots, combined our results with them, and show the results in Figures 17 and 18. Our calculations for these figures use RQ 36 parameters except we used a one-meter radius sphere, and a period of 24,704,000 seconds in Figure 17 and a period of 24,040,000 seconds in Figure 18. Sekiya et al.[6] use global parameters in their results so our periods were chosen to put our results on the same scale as theirs. Looking at Figure 17 we see that our result at $\phi = 0^o$ and $\theta = 60^o$ is similar to that of Vokrouhlický. However, away from center, our results are warmer, but again resemble Vokrouhlický's on the nightside. On the other hand at $\phi = 0^o$ and $\theta = 120^o$ our results are definitely warmer than those of Sekiya, et al. and of Vokrouhlický, but drop off more sharply near the limb. On the nightside for 120^o our results are similar to those of Sekiya, et al. and Vokrouhlický's results are clearly warmer than the other two results. Figure 18 shows a delay in heating, but otherwise the relative relationships between the three sets of results remain the same as in Figure 17. Our temperature results are always greater than or equal to, the results of the other authors in the sunlit region.

VII. Conclusions

The numerical solutions given by the COMSOL Multiphysics software are in reasonable agreement with previously published results and are quite possibly more correct since there are no theoretically built in approximations. We showed how the Yarkovsky effect is related to the size, period of rotation, and obliquity of a sphere having thermal conductivity of 0.3, density of 2000, and heat capacity of 600 at a distance of 1 AU from the sun. Approximating the asteroid RQ 36

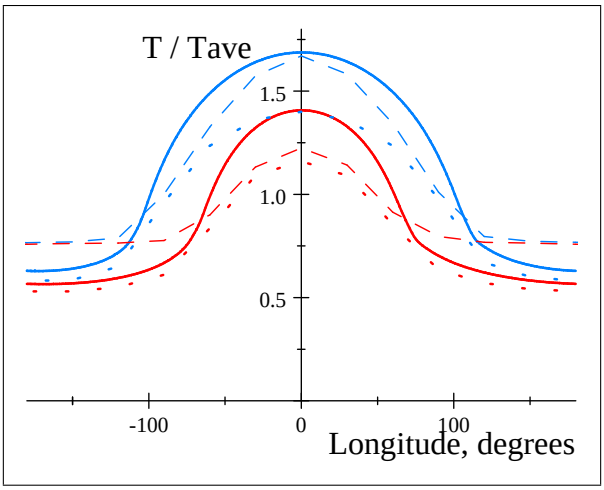

Figure 17. Plot of temperature distribution for latitudes 60 degrees (blue) and 120 degrees (red). Solid line is from COMSOL results, dotted line from Sekiya et al, and dashed line from Vokrouhlicky.

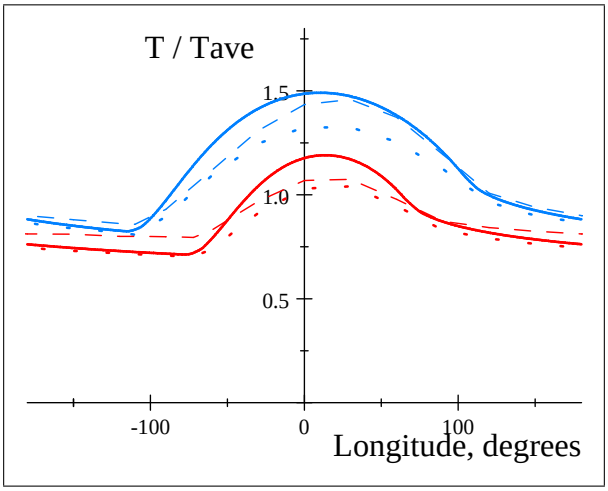

Figure 18. Same as figure 17, but with a thermal lag.

as a sphere of homogenous composition, the Yarkovsky force is 0.0843 N. With the flexibility of COMSOL in the future it will be possible to evolve the spherical homogeneous model into more realistic versions of an asteroid. The seasonal effect due to orbital motion can be included as well. The work reported here is in a preliminary stage. We will continue with extensive modeling and determining changes in orbital parameters due to the Yarkovsky effect. These results will contribute towards improving predictions of orbital changes of near-Earth objects (NEOs). One of the objectives of NASA's OSIRIS-Rex mission (to be launched in 2016, to reach the asteroid in 2020, and return samples to Earth in 2023) is to directly measure its Yarkovsky acceleration. With improved measurements of the physical properties of RQ 36 and refinement of analytical and numerical techniques, accuracy of predicted forces will steadily improve for many (NEOs).

VIII. Acknowledgments

We thank Ikenna C. Niebedim for significant assistance with setting up COMSOL jobs. We also thank Mian Qin from COMSOL for helping us with the swept mesh analysis.

References

[1]Milani, A.,Chesley, R. C., Sansaturui, M. E., Bernardi, F., Valsecchi, G. B., and Arratia, O., "Long Term Impact Risk for (101955) 1999 RQ_{36}," *Icarus*, Vol. 203, 2009, pp. 460-471.

[2]Farinella, P., Vokrouhlický, D., and Hartmann, W. K., "Meteorite Delivery via Yarkovsky Orbital Drift," *Icarus,* Vol. 132, 1998, pp. 378-387.

[3]Vokrouhlický, D.,"A Complete Linear Model for the Yarkovsky Thermal Force on Spherical Asteroid Fragments," *Astron. Astrophys.,* Vol. 344, 1999, pp. 362-366.

[4]Bottke, Jr.,W. F., Rubincam, D. P., and Burns, J. A., "Dynamical Evolution of Main Belt Meteoroids: Numerical Simulations Incorporating Planetary Perturbations and Yarkovsky Thermal Forces," *Icarus*, Vol. 145, 2000, pp. 301-331.

[5]Žižka, J., and Vokrouhlický, D., "Solar Radiation Pressure on (99942) Apophis," *Icarus*, Vol. 211, 2011, pp. 511=518.

[6]Sekiya, M., Shimoda, A. A., and Wakita, S., "An Iterative Method for Obtaining a Nonlinear Solution for the Temperature Distribution of a Spinning Spherical Body Irradiated by a Central Star," *Plan. Space Sci.*, Vol. 60, 2012, pp. 304-313.

[7]Rozitis, B. and Green, S. F., "Directional Characteristics of Thermal–Infrared Beaming from Atmosphereless Planetary Surfaces–a New Thermophysical Model," *Mon. Not. R. Astron. Soc.*, Vol. 415, 2011, pp. 2042-2062.

[8]Rozitis, B. and Green, S. F., "The Influence of Rough Surface Thermal–Infrared Beaming on the Yarkovsky and YORP Effects," Vol. 423, 2012, pp. 367-388.

[9]http://www.comsol.com/.

[10]Vokrouhlický, D., "Diurnal Yarkovsky Effect as a Source of Mobility of Meter-sized Asteroidal Fragments: I. Linear Theory," *Astron. Astrophys.*,Vol. 335, 1998, pp. 1093-1100.

[11]Jackson, J. D., *Classical Electrodynamics*, 2nd ed., John Wiley & Sons, 1975.

[12]Schott, J. R., *Remote Sensing: The Image Chain Approach*, Oxford Univ. Press, 1997.

[13]Delbo, M. and Michel, P., "Temperature History and Dynamical Evolution of (101955) 1999 RQ 36: A Potential Target for Sample Return from a Primitive Asteroid," *Astroph. J. Lett.,* Vol. 728, 2011, pp. L42-L46.